Engineering Fracture Mechanics 291 (2023) 109544

Contents lists available at ScienceDirect

Engineering Fracture Mechanics

journal homepage: www.elsevier.com/locate/engfracmech

Fatigue behavior of 316L stainless steel fabricated via Material Extrusion Additive Manufacturing

Saveria Spiller, Sondre Olsøybakk Kolstad, Nima Razavi *

Department of Mechanical and Industrial Engineering, Norwegian University of Science and Technology, Richard Birkelands vei 2B, 7491 Trondheim, Norway

ARTICLE INFO

Keywords:
Material Extrusion Additive Manufacturing
Steel
Fatigue life
Porosity

ABSTRACT

Material Extrusion Additive Manufacturing (MEAM) is a novel technique that widens the field of additive manufacturing applications in producing metal parts. There is limited knowledge about the process-induced properties of the metal parts obtained with such a process, especially when dealing with cyclic loading. The present work aims to assess the fatigue life of 316L components fabricated via MEAM, investigating the fatigue failure mechanisms. The resulting S-N curve shows a lower fatigue limit compared to wrought 316L. Internal defects are detrimental to the fatigue life since crack initiation sites are observed from the pores resulting from the deposition strategy of the material during the printing phase.

1. Introduction

The production of metal parts via additive manufacturing is an increasing trend for several industrial applications, in particular in the automotive, aerospace, and biomedical fields [1,2]. The advantages of AM are mainly related to the freedom of design and the possibility of producing single or small batches of parts, reducing material waste. Nevertheless, there are well-known limitations especially in terms of economy and safety issues [3]. The additive manufacturing processes referred to as powder bed fusion techniques (PBF) such as L-PBF, and EB-PBF are the most used techniques in metal production [4]. These techniques need expensive and advanced facilities, and high-power sources to maintain the laser or electron beam. Severe safety issues must be addressed, especially regarding the large quantity of metal powder to be handled. These challenges and drawbacks are hindering the diffusion of PBF in the industry [3,4].

In this scenario, innovative techniques such as Material Extrusion Additive Manufacturing gains interest in the scientific and industrial community. The advantages of MEAM in terms of costs and safety issues are related to the fabrication process described in the following sections, which is conceptually different from the PBF techniques, requiring less sophisticated equipment. At the same time, the process-induced properties of the parts produced via MEAM are different from PBF parts and require proper investigation and understanding.

Material Extrusion Additive Manufacturing (MEAM from here on) is a multiphase technique that is referred to with several denominations, such as MEX, FDMet, or SDS [5–7]. A schematic illustration of the process is depicted in Fig. 1. The feedstock material is a composite material named highly filled polymer (HP) since it is composed of metal powder dispersed in a polymer matrix [5]. The mixture is usually blended and extruded in the shape of a filament, but it is also possible to compose the material in pellets or rods.

* Corresponding author.
E-mail address: nima.razavi@ntnu.no (N. Razavi).

https://doi.org/10.1016/j.engfracmech.2023.109544
Received 29 June 2023; Received in revised form 10 August 2023; Accepted 11 August 2023
Available online 12 August 2023

Nomenclature

AM	Additive Manufacturing
BJ	Binder Jetting
EB-PBF	Electron Beam Powder Bed Fusion
FDM	Fused Deposition Modeling
FDMet	Fused Deposition Modeling of Metals
HCF	High Cycle Fatigue
HIP	Hot Isostatic Pressing
HP	Highly filled Polymer
L-PBF	Laser Powder Bed Fusion
MEAM	Material Extrusion Additive Manufacturing
MEX	Material Extrusion
MIM	Metal Injection Molding
PBF	Powder Bed Fusion
SDS	Shaping, Debinding, Sintering
SS	Stainless Steel
UTS	Ultimate Tensile Strength

Several metallic materials have been used so far with this process: stainless steels 316L [7–15] and 17-4PH [16–21]; titanium [22–25]; hard metals and tungsten [26,27]; and copper [28]. Beside metallic materials, ceramic powder [29] and combined ceramic and metal powder [30] can also be used in the feedstock of this process to produce ceramic and metal-ceramic composite parts.

The required equipment for this process includes an FDM printer or an apparatus with similar features. The filament is softened, extruded through a nozzle, and selectively deposited with a layer-wise strategy to build the part. This is the first phase of the process, called printing or shaping phase. The outcome of the printing phase is referred to as green part, it is a composite material with poor mechanical resistance. Mechanical and physical characteristics of green parts have been widely investigated, since the quality of the final sintered parts is strongly dependent on the result of the printing phase. Examples of green parts' tensile characterization can be found in [19,31]. To obtain a pure metal part, the binder is removed after the shaping phase, through a process called debinding. Thermal, solvent, or catalytic debinding has been successfully performed, depending on the polymers used in the feedstock materials

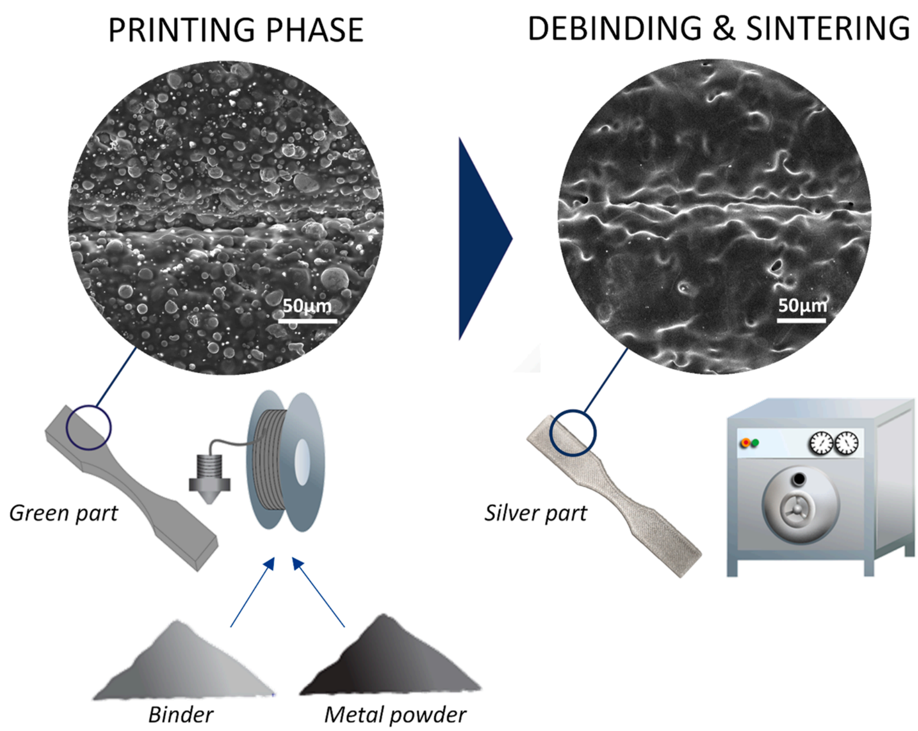

Fig. 1. A schematic of the MEAM process with magnifications of the highly-filled polymer with visible spherical metal particles in green part and the sintered metal in silver part.

[5–7]. The process allows the binder to dissolve and flow away from the part. After this phase the part is called brown part: it consists of metal powder packed together and this is the most fragile state of the printed parts. Finally, the parts are sintered.

Sintering is a well-known metallurgical process, in which the increasing temperature and pressure allow the metal atoms to diffuse, creating necks between the powder particles that bond together and densify the part [32]. The final part is usually called silver part. There are other established manufacturing processes where debinding and sintering are required. This is the case of metal injection molding and binder jetting additive manufacturing. The microstructure of parts produced with the abovementioned techniques is indeed similar, characterized by equiaxed grains and isotropic coarse microstructure. Nevertheless, the fabrication challenges differ widely from process to process.

The number of parameters involved in MEAM is wide. In every step of the process, the parameters can affect the microstructure, porosity, and density of the final parts, and consequently their mechanical properties. Some of the main parameters of the printing phase are nozzle temperature, layer thickness, printing speed, cooling fan speed, flow rate multiplier, and printing strategy [33]. For both debinding and sintering, the most relevant parameters are the temperature and the dwelling time. The atmosphere in the furnace is important as well, for example, it is beneficial to use inert gases to avoid oxidation of the parts. Proper tuning of all these parameters is fundamental for the quality of the final part. Indeed, several researchers were focused on the optimization of the process, sometimes using robust techniques such as Taguchi orthogonal arrays [19].

The relation between fabrication parameters and mechanical properties of the silver parts is important. As already mentioned, so far, most part of the works available in the literature about stainless steel parts fabricated via MEAM are focused on the assessment of the effect of the printing parameters on the static tensile or bending properties of the silver parts [12–15,34]. The fatigue behavior of the parts has not been thoroughly investigated yet, with only a few studies recently available in the literature [8,35,36].

The fatigue behavior of a metal component depends on multiple internal and external factors. Characteristics such as microstructure, surface roughness, and porosity have an important impact on the fatigue life of a specimen. These features are process induced, often difficult to predict with precision, and dependent on the employed process parameters [37,38]. For example, in [39] the fatigue life of specimens produced with L-PBF and BJ are compared. L-PBF parts performed significantly worse, and the main reason is attributed to the microstructure features that are not able to act as a barrier for the dislocation movement. It is well known that PBF techniques in general entail steep thermal gradients that affect the microstructure of the part, promoting an anisotropic fine cell structure and elongated columnar grains, increasing the hardness and strength of the components while decreasing the ductility [40–43]. BJ, on the other hand, relies on a different working principle since the green parts are shaped out of metal powder bound together with glue, and subsequently debinded and sintered to achieve the final result. In this process no rapid heating is involved, therefore residual stresses and anisotropy in the microstructure are not promoted. The grains are in general coarser in comparison with PBF parts, and equiaxed. The absence of tensile residual stresses, contrary to PBF parts, is an advantage since they can be detrimental in the nucleation phase of a crack [37]. As already mentioned, MEAM parts are characterized by equiaxed and coarse grain size [13,35], indeed similar to BJ parts, leading to the expectation of similar mechanical behavior. Indeed, other factors can affect the fatigue life of AM components. For example, surface defects can act as possible crack initiation sites. In [36] a comparison between the fatigue life of L-PBF and MEAM 316L parts is offered, showing that the fatigue strength of MEAM is lower. The higher surface roughness is considered responsible for the result. Nevertheless, pores and internal defects can be more detrimental than superficial flaws as found in [42], a study about the fatigue life of L-PBF 316L parts. While for PBF techniques typical internal defects are lack-of-fusion, inclusions, or gas-porosity [37,38], the residual porosity in MEAM can be divided into two categories, porosity originating from the printing phase and from the sintering process [15]. These characteristic features of MEAM parts are carefully considered when assessing the fatigue life of the specimens.

The present work aims to investigate the fatigue behavior of 316L SS specimens produced via MEAM. In section 2 the materials and

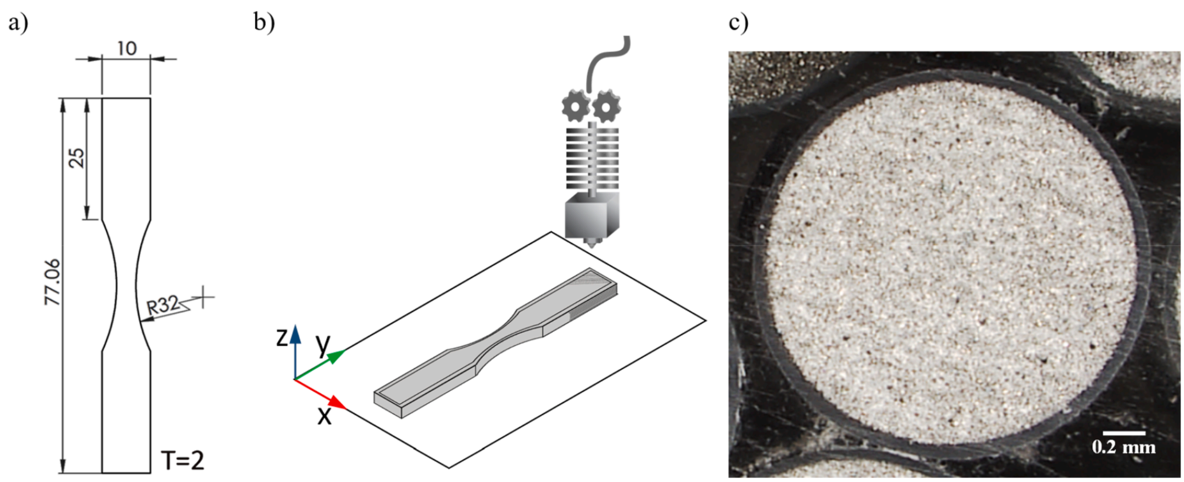

Fig. 2. a) Desired dimensions of the silver parts. all the dimensions are in mm; b) flat printing orientation adopted in the present work, the building direction correspond to z-axis; c) cross section of the filament BASF Ultrafuse 316L. The diameter of filament is 1.75 mm.

methods adopted for the production and characterization of the specimens are described. Section 3 reports results for superficial and internal analysis such as roughness assessment, Vickers microhardness, and porosity evaluation. Section 4 is fully dedicated to the fatigue test results covering also a comparison of the findings with other works on fatigue properties of the studied material. Fractography was used to evaluate the failure mechanisms of the tested specimens under fatigue loading. Finally, discussions and conclusions are presented in sections 4 and 5.

2. Materials and methods

2.1. Fabrication process

The hourglass-shaped specimens were designed according to the ASTM standard E466-21 with the dimensions shown in Fig. 2a. The FDM printer used was a commercial Prusa i3 MK3S and the specimens were printed flat on the printing platform, as depicted in Fig. 2b. This building orientation does not require support material. The filament used is the BASF Ultrafuse 316L, available on the market. It contains > 80 wt% of 316L stainless steel metal powder. A cross-section of the filament is shown in Fig. 2c. The SS particles are mainly spherical and the diameter ranges between 4 and 40 μm. With respect to the actual size desired, the dimensions of the specimens' model were increased to compensate for the shrinkage that occurs during the sintering process. The shrinkage factors suggested by the filament producer are 19% and 21%, respectively along the x-y plane and the z-axis of the building platform. As mentioned, test specimens were printed horizontally, flat on the printing platform, with 100% infill density. The layer thickness was set to 0.1 mm and rectilinear infill pattern with 45/-45° raster angle. This is a typical strategy used for the inner part of FDM parts, as to say the infill rasters. It is beneficial to surround this core with outer contour walls, as visible in Fig. 2b, to improve the shape retention of the parts. In our case, three contour walls were printed. Due to the metal powder content in the HP filament, the printing phase is more challenging than for a regular polymeric filament, such as PLA, and special strategies were adopted. To ensure a stable and consistent extrusion flow, the printing temperature was held to 295 °C, close to the safety limit of the printer. This is significantly higher considering that to print PLA the suggested nozzle temperature ranges between 180 °C and 230 °C [44].

Another issue during printing was related to the adhesion of the green part to the platform. The printing platform temperature was held to 100 °C and a brim was printed along the specimens to avoid warpage, as suggested in [45]. Only for the first layer deposition the cooling fan was kept off and the thickness was increased to 0.15 mm to facilitate the extrusion and the consolidation of the softened material on the platform. The cooling fan speed was then immediately increased to help the shape retention of the green part and improve the external appearance. Another helpful action for higher geometrical accuracy was reducing the printing speed during the deposition of the outer contour. As reported in [19], it is in general beneficial for the density and therefore strength of the green part to increase the quantity of material extruded per second. The parameter regulating this aspect is usually called flow rate multiplier. Nonetheless, it was found that even small variations of this parameter have a detrimental effect on the external surface, resulting in more irregularities and defects. Other strategies can be adopted to improve the cohesion of infill, for example increasing the overlap of adjacent rasters, as described in [31].

After the printing phase, debinding and sintering of the green parts were outsourced to an appointed company, Elnik Systems GmbH. According to the filament datasheet, a catalytic debinding is performed at 120 °C with HNO_3 followed by the sintering cycle performed in H_2 or Ar_2. The specimens are heated up to 600 °C for 1 h, then to 1380 °C for 3 h, and finally furnace cooled.

2.2. Shrinkage of the silver parts

The silver parts were analyzed and investigated to assess the overall quality of the process. First, the linear reduction of the specimens' dimensions was measured with a caliper to evaluate the shrinkage of the parts due to the sintering process. The percentage of reduction was calculated as the relative difference of green parts (d_g) and silver parts (d_s) dimensions: $(d_g\text{-}d_s)/d_g$. The shrinkage of sintered compacts of metal powder is due to the neck growth between particles that determine a dimensional change. Progressively, the contact areas between particles become grain boundaries that tend to expand. The coarsening of the grains is induced by the sintering temperature, and while the grains growth, the pores shrink. The final density of the silver part depends on the density of the powder compact before sintering [46].

2.3. Roughness assessment

The surface roughness was also assessed using the optical microscope ALICONA InfiniteFocus SL, provided with a 3D tool for roughness measurements. The surface imperfections have an important role in the fatigue life of metal components since cracks easily nucleate from superficial defects [37], therefore the arithmetic average roughness value R_a was measured on the side (i.e., along the thickness), top, and bottom surfaces of the specimens.

2.4. Residual porosity evaluation

Besides the superficial features of a metal part, internal defects and porosity are also detrimental for the load-bearing capacity and fatigue life time of a component [37]. To evaluate the internal defects of the printed parts, some cross sections were cut from the silver parts with a sewing machine, embedded in resin, ground from 220 to 2000 grit, and polished from 6 to 3 μm. The cross sections were observed with the digital microscope Hirox rH2000. The pictures were then analyzed with the graphic software Image J to measure the pores' extension within the bulk.

2.5. Microstructures and microhardness investigation

The polished cross-sections were etched with a solution composed of 10 ml H_2O, 10 ml HCl and 1 ml of HNO_3 to allow a microstructural evaluation of the metal and measure the grain size. This etchant was proved to be effective on 316L in [39]. Ultimately, one of the sections was also used for Vickers microhardness tests, using the Mitutoyo Hardness machine MicroWidZhard HM-200 series. To evaluate possible hardening effects on the contours in comparison to the infill of the specimens, multiple indentations were taken from the edge to the center of the cross-section at three different heights.

2.6. Uniaxial fatigue tests and fractography

Uniaxial fatigue tests were performed with the testing machine Instron Electropulse 10E equipped with a load cell capacity of 10kN. The frequency of the sinusoidal waveform was set to 20 Hz, and the cyclic loading was performed with a loading ratio of $R = 0.1$. Specimens surviving 2 million cycles were considered run-outs. The fractured surfaces of the specimens were observed with the SEM FEI QUANTA 650 FEG to better understand the failure mechanisms.

3. Results

3.1. Shrinkage of the silver parts

The thickness, width, and length of the silver parts were measured using a caliper, and the dimensional reduction in percentage was calculated. The shrinkage values obtained were respectively 18.7%, 17.3%, and 20.7% along the x, y, and z-axis, as shown in Fig. 3a. As previously mentioned, the shrinkage of sintered metal powder compacts is related to the atomic diffusion of the particles, and it depends on the initial density of the green part. In the case of MEAM parts, the material deposition strategy affects the density of the green parts since voids are usually left between adjacent strands, on the intersection of infill and contours, and on the interfaces of the layers. According to [12], the motion of the nozzle determines a dragging force on the binder, leading to a poor concentration of powder in the layer interface, as depicted in Fig. 3b. After the debinding, these areas become voids, resulting in higher compaction of the part along the building direction. Gravity might also play a role in the vertical collapse of the powder after the debinding [47]. Moreover, the shrinkage reported in the present work is in line with what was found in other similar studies. For example, in [13] the shrinkage is reported to be 16.5, 19.2, and 21.1 % respectively on the x, y, and z-axis.

3.2. Roughness assessment

The surface roughness was measured in the three different areas indicated in Fig. 4. On the top surface of the specimens, an average

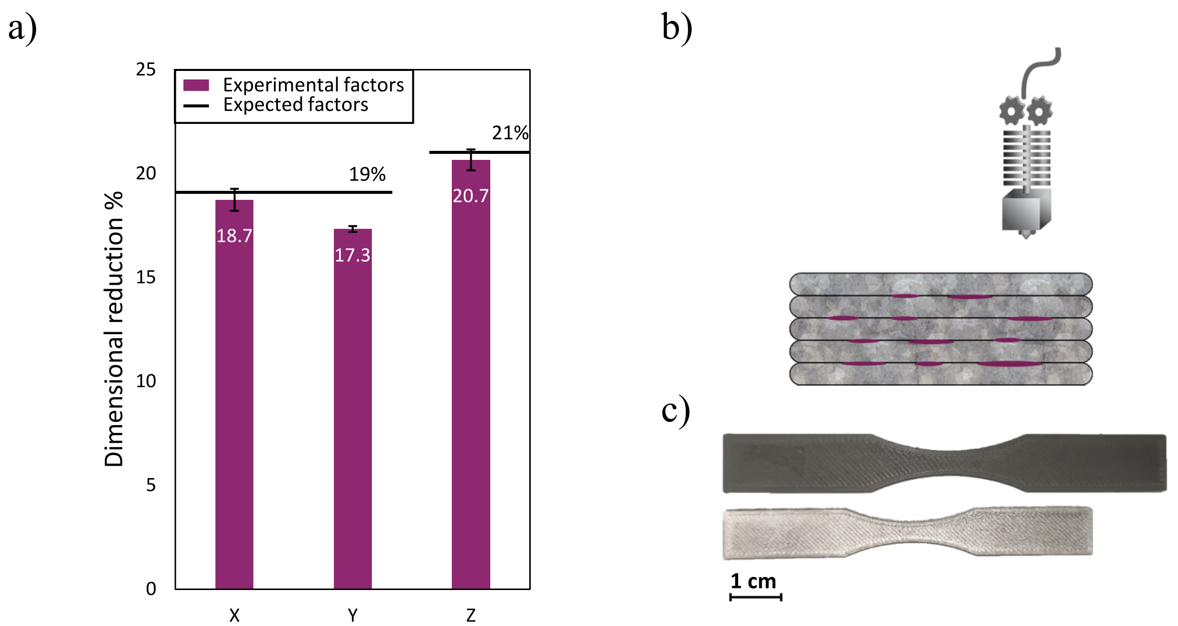

Fig. 3. a) Shrinkage factors obtained, and target factors expected [48]; b) layer deposition strategy and elongated areas with high concentration of binder along the layers interfaces; c) difference in size between the green part and the silver part.

Ra of 5.96 ± 0.15 was found. Due to the building orientation, the top and bottom surfaces of the specimens appear significantly different: the bottom surface is constantly in contact with the heated printing platform during the printing process, which induces a smoother surface where the nozzle path is less evident. Nevertheless, during the sintering process, some defects appear, increasing the average roughness that was measured as Ra 5.04 ± 1.80. The roughness on the side of the specimens was also assessed, even though, due to the limited thickness, the evaluation length was shorter and therefore the measures are less accurate. The average Ra obtained is 7.70 ± 0.53.

3.3. Residual porosity evaluation

As shown in the schematic in Fig. 5a, sections A-A, B-B, and C-C were analyzed to evaluate the porosity shape and distribution. It was previously mentioned that there are two types of porosity affecting MEAM parts [15]: relatively bigger pores are due to the deposition strategy of the material, and they appeared in specific locations, where adjacent rasters conjoint. On the other hand, smaller round pores with a diameter of a few microns are randomly distributed and derived from the sintering process. An SEM picture representing clearly this difference is presented in section 3.7, detail III in Fig. 10a. In Fig. 5, optical microscope pictures are presented with a magnification such as only the porosity induced by the printing strategy is visible. Due to the tridimensionality of the pores, volumetric measurement techniques such as CT scan of the specimen will allow measurement of the real volume of pores. Increasing the number of grinding steps, the porosity in the cross-sections changes, therefore the quantitative data extrapolated in this section has the value of giving a rough idea of the porosity induced by the printing phase.

Section A-A represents the gauge cross-section which is the smallest in terms of thickness. Pores appear to be quite irregular in the shape, with a precise distribution that follows the deposition strategy. The average equivalent diameter of the pores observed in this section is 37.2 μm, even though the variability is significant, with a minimum size of 8.3 μm and a maximum of 118 μm. The porosity is estimated at 1.61% of the total area of that section.

Sections B-B and C-C have a similar appearance. The pore distribution is clearer and similar to section A-A, with the average size of 37.5 μm. The pictures give several information about the distribution of the pores. The outer walls are more compact in comparison to the infill. This is clear especially from section A-A and B-B. It can be attributed to the chosen printing parameters: the outer walls were printed along the outer boundary of the geometry with reduced speed with respect to the infill to increase the accuracy of the external surface. This enabled a better flow of the material. Moreover, the infill is overlapping the internal wall to increment the compactness of the specimen, which is clearly a successful strategy. The bottom part of each section is denser, and in section A-A and B-B it is also visible what looks like the so-called 'elephant toe' defect, typical of FDM parts, which consists in poor shape retention of the bottom layer of a part that deformed because of the weight of the upper layers [45]. In the case of MEAM, the densification of the bottom part is not only due to the weight of upper material during the printing phase but it is also likely that the proximity with the hot printing bed (kept at 100 °C) helped the material adhesion in the lower layers. Besides the average equivalent diameters of the pores is consistent in every sections, the pores in section A-A are more irregular and deep, since it is almost impossible to grind the section to a depth in which the pores disappear. This can be explained considering the wider size of sections B-B and C-C: on one side the larger width allows a slower heat dissipation in the layers deposited, favoring the bonding between rasters. On the other side, an effect due to the printing speed has probably occurred. In [49], it was observed that the pores are smaller near the turning points of the nozzle in comparison to the center of the infill. Where the nozzle changes direction, it decelerates to stop and invert its speed. Section A-A being narrow, the nozzle decelerates and accelerates continuously in a relatively short distance, meaning that the acceleration magnitude is high. This affects the deposition of the softened material and consequently the pore's size.

3.4. Microstructure investigation

The material grains were exposed by etching the polished samples with the reagent described in the previous section. As expected, the microstructure appears to be equiaxial (Fig. 7a). This is the typical microstructure of annealed stainless steels, that have not experienced steep thermal gradients. Many twinning defects are visible: these linear defects are typical features of austenitic steel, and they are consequences of deformation experienced by the sample. The grains' size was measured with the software Image J. The

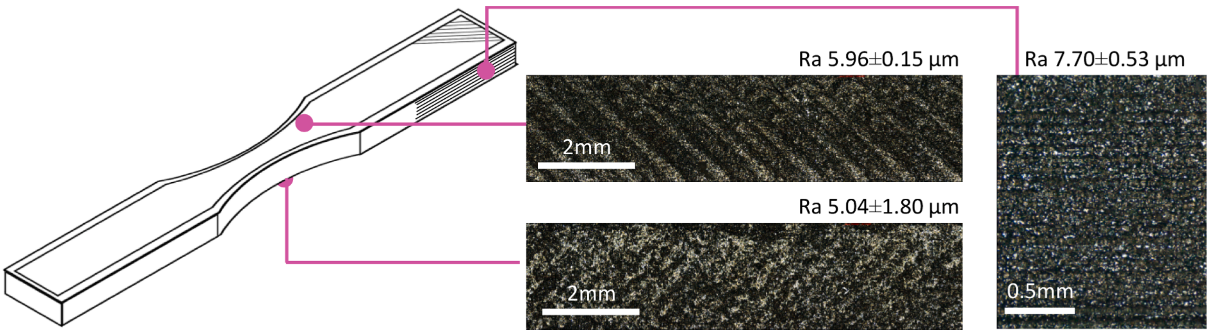

Fig. 4. Magnification of the top, bottom, and side surfaces of the specimen with the corresponding values of Ra [μm].

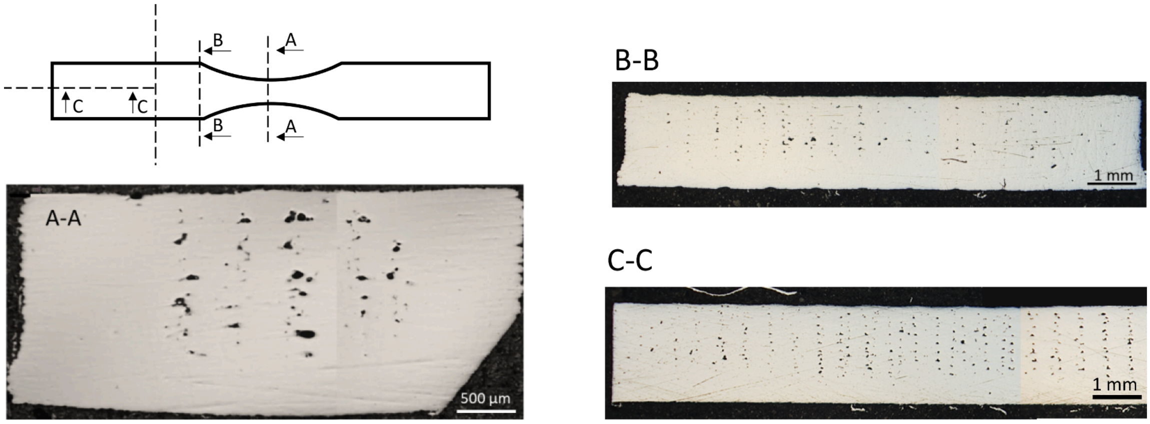

Fig. 5. Schematic of the sections cut and polished from the fatigue specimen: A-A is the gauge section; B-B is the grip section; C-C is the longitudinal section. In all the section regular circular pores are observed. The pores distribution is not random since the location of voids follow the path of the nozzle during the deposition of the material in the printing phase.

average grain diameter is 43.9 ± 0.9 μm, a value in line with what is typical for sintered 316L stainless steel [35]. What is worth noting is the relative size of the grains with respect to other features in the pictures: in Fig. 7b, it is possible to observe that the grains are in some cases larger than the deposition-induced voids. Fig. 7c represents the side edge of a cross-section, with the typical ladder pattern obtained with the superposition of layers. The overhangs are sometimes exactly the size of a grain.

3.5. Microhardness tests

As mentioned before the Vickers microhardness has been measured on the section B-B. To evaluate properly the variation of the microhardness through the thickness and the width of the specimens, indentations have been made along three parallel lines to assess possible differences between the core of the specimens and the top and bottom surface. With the same purpose, multiple indentations were taken for each line from the external surface to the center of the section. The scatter among data is limited and no significant variations in the hardness were observed between the specimens' core and contours. What was noticed is that indentations too close to pores resulted in considerably lower hardness values that were therefore not considered representative. The average value, depicted with a pink continuous line in Fig. 6 is HV 204. A reference value of the Vickers microhardness of wrought 316L [50] is reported with a blue dashed line at it is HV 222, slightly above the result of the present work.

3.6. Uniaxial fatigue tests

Uniaxial fatigue tests results are presented in Fig. 8. The focus of the current work being HCF, the specimens that failed at less than 10^4 cycles were excluded from further statistical analysis since this is the conventional boundary between low and high cycle fatigue. Three specimens, marked with an arrow in Fig. 8, met the run-out conditions exceeding 2 million cycles. The scatter bands were calculated referring to a 90% probability of survival at a confidence level of 95%, according to the procedure described in the standard ISO 12107. The scatter index, calculated as $T_\sigma = \sigma_{10\%} / \sigma_{90\%}$, is a parameter used to assess the dispersion of the data. In the present work the index obtained is $T_\sigma = 1.9$, that indicates limited scatter in the data. The inverse slope of the fatigue curve obtained in double logarithmic scale is k = 4.47. According to the plot, the run-outs can be represented properly by the dashed line that depicts a knee at

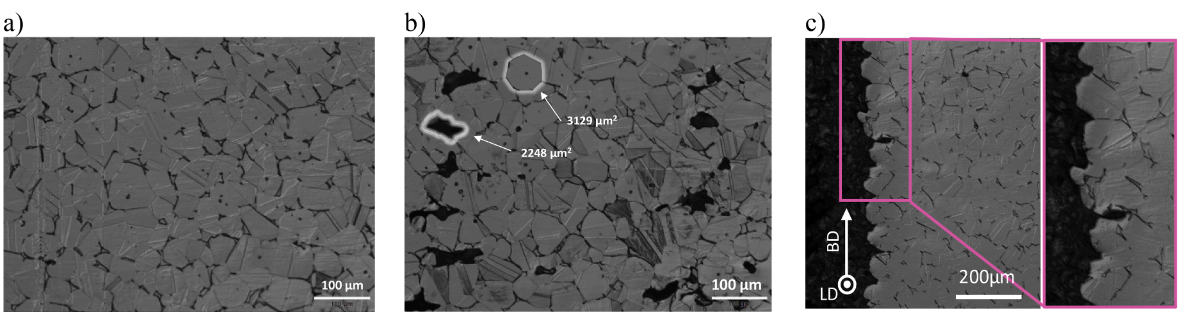

Fig. 6. a) Grain boundaries exposed in the etched sample. Twinning defects are visible in many grains. b) comparison in dimension of a pore and a grain to highlight the coarse microstructure; c) magnification of the side of the specimen. BD stands for building direction and LD for loading direction.

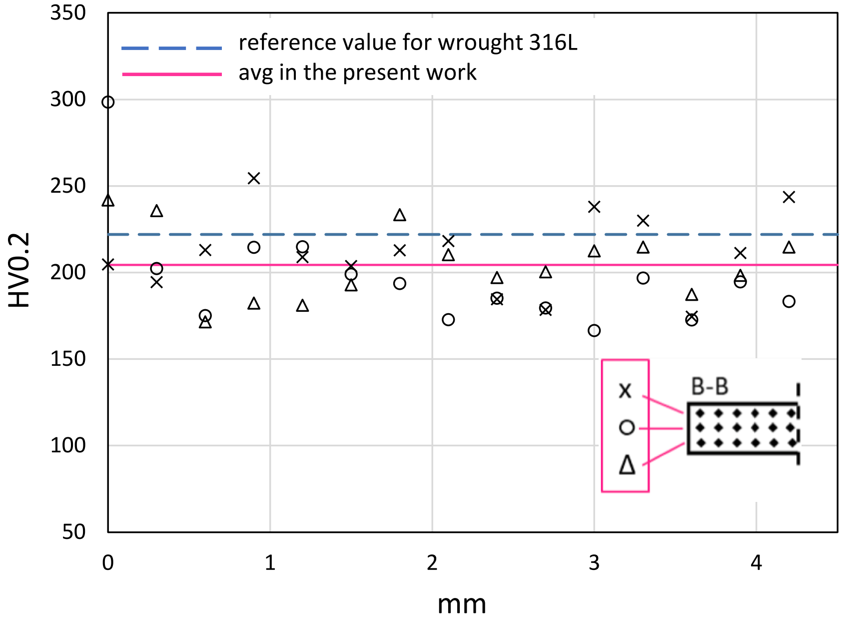

Fig. 7. Vickers's microhardness results. In the bottom right corner of the plot, a schematic of the distribution of indentations is shown. Multiple measurements were performed along three lines through the thickness, from the side edge to the middle of the width of the cross-section. A pink continuous line indicates the average value found in the present work, while a blue dashed line shows a reference value of HV reported in [50] for wrought 316L.

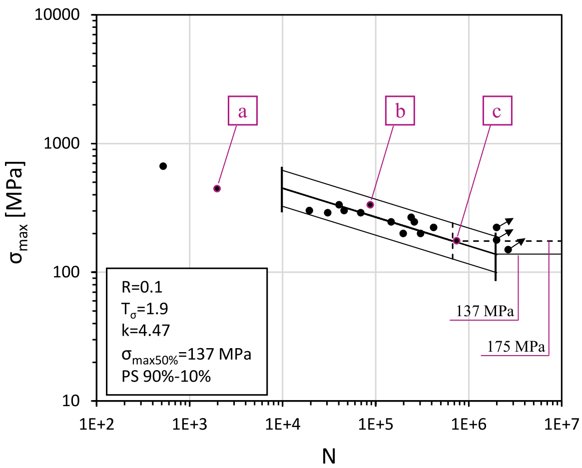

Fig. 8. Fatigue data from MEAM 316L specimens tested under loading ratio of R = 0.1 and 20 Hz loading frequency. The specimens marked with the letters a, b, and c are further analyzed in the fractography section.

175 MPa. The conventional value $\sigma_{max50\%}$ obtained statistically is 137 MPa. Three specimens indicated with the letters *a*, *b*, and *c* are considered in the fractography section.

To collocate these results in a wider frame, Fig. 9 shows the comparison between the specimens fabricated and tested in the present work with other data collected from the literature that refer to both wrought 316L SS and other MEAM specimens. All data were converted to R = 0.1 using the SWT correlation [51]. From the plot, it is possible to notice a clear distinction between additively manufactured and wrought materials. It was considered useful to schematically highlight the areas in which the two groups of data lay, with yellow background for MEAM and green for wrought. As expected, MEAM fatigue data occupy the lower part of the plot, while wrought 316L shows higher fatigue strength, up to an equivalent maximum stress of 500 MPa [52–54]. In [52,54] respectively, superficial treatments were performed to increase the fatigue limit of the wrought material: superficial mechanical attrition treatment (SMAT), and superficial mechanical rolling treatment (SMRT). Surprisingly, the data obtained in [54] for wrought material appear to be in line with the data obtained in the present work.

With regard to the other works related to MEAM, the fatigue limit obtained in the present works is higher in comparison to the

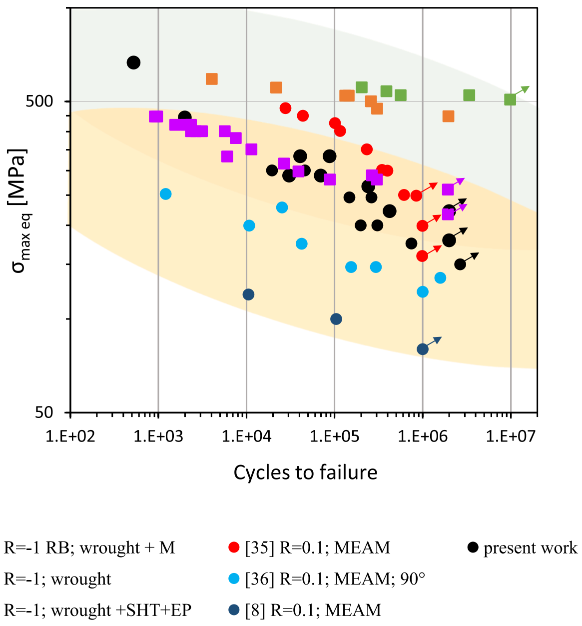

Fig. 9. Fatigue data from MEAM 316L specimens and wrought 316L reported in terms of maximum equivalent stress calculated with SWT correlation. In the legend, the loading ratio is reported as well as the manufacturing method (MEAM or wrought) and post treatment operations. RB = Rotating bending test; M = machined; EP = Electropolished; SHT = Solution Heat-Treatment; 90°=vertical building orientation. Different background colors were used to highlight the partition of the plot area: wrought 316L (green background) is characterized by a higher fatigue limit, while MEAM components (yellow background) occupy the lower part of the plot.

results reported in [8] and [36]. In [36] the fatigue specimens were printed with a vertical orientation, meaning that the building direction was parallel to the load line during the uniaxial fatigue tests. This is known to be detrimental when dealing with AM since the building direction offers the weakest resistance also in static tensile tests [12,20,21]. Besides this, the discrepancy between the other works is possibly related to the different process parameters involved in the fabrication process of the specimens.

3.7. Fractography

SEM pictures of the fracture surfaces were taken to gain knowledge about the failure mechanisms and the defects that led the specimen to failure. Fig. 10 represents SEM pictures belonging to three specimens that have been selected to cover properly the studied fatigue life range, from high to low stress levels.

Fig. 10**a** shows the fracture surface of specimen *a* (see labels in Fig. 8). The specimen failed at less than 10,000 cycles, at a stress level close to the tensile strength measured on dogbones obtained with the same process parameters reported in [31]. The fracture surface shows indeed mainly ductile fracture features, with dimples and coarse surfaces extended to most of the area, especially in the core. Only the outer surfaces corresponding to the contour walls of the specimens show signs of stable fatigue crack growth. With closer observation, for example in the top left corner (I), it is possible to assume that the crack started from the inside of the specimen, where large voids created unbearable stress intensification. Indeed, the pore distribution is perfectly shown in the picture. It has been already explained that there are two possible origins for the pores in MEAM specimens: the first is related to the deposition pattern. The interface between walls and infill is clearly marked by a row of spherical voids (detail II). Furthermore, in the core, wide coalescent pores have formed vertical "rivers" proving poor adhesion between rasters within the same layer. The layers interfaces are less evident, meaning that the sintering process promoted good densification along the building direction. This was expected considering the higher value of the shrinkage along the thickness of the specimens. Besides this "macroporosity", it is possible to observe a sort of "microporosity", with smaller circular pores distributed randomly on the surface (see detail III). These pores are due to the sintering process and are the result of a lack of densification of the metal powder [48].

Fig. 10**b** shows the fracture surface of the specimen *b*. Here brittle fracture features, typical of the fatigue crack propagation, are more visible. Again, multiple crack fronts seem to start from the internal macro pores, propagating toward the outer surface. In detail I, a flat fracture surface indicates the propagation of a fatigue crack in the center of the specimen. Fig. 10**c**, showing specimen *c*, indicates the same trend. In this case, three separate fatigue propagation areas are discernible in the core of the fracture surface. The cracks propagate towards the outer surface, where the ductile features of the final disruptive fracture are clear. In detail I, a crack initiation point is shown. The macro pore from which originated is also highlighted.

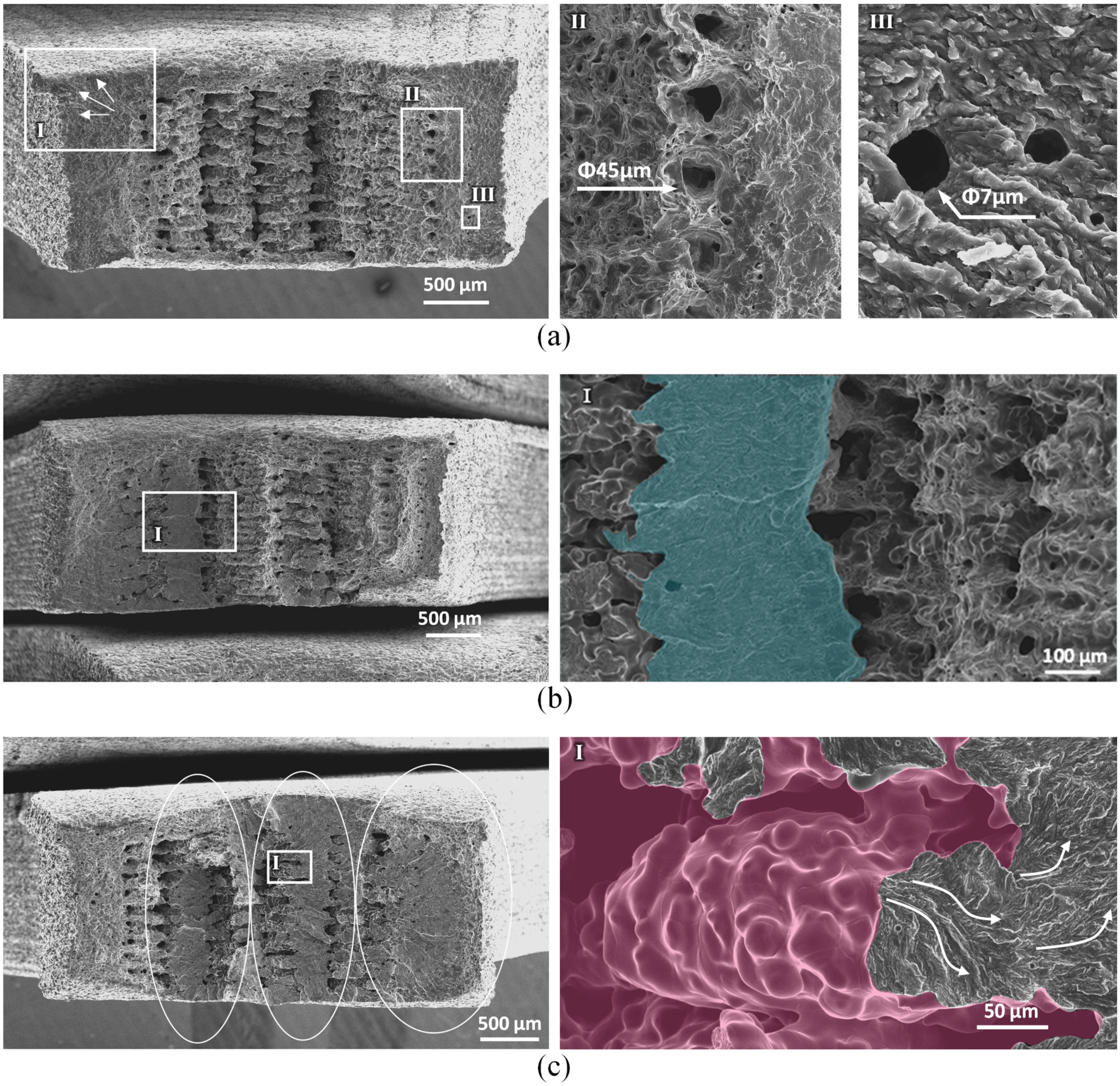

Fig. 10. SEM pictures of fracture surface of three fatigue specimens broken respectively at a) high stress, b) medium stress, and c) low stress, close to the fatigue limit.

4. Discussion

The fatigue life of 316L MEAM specimens appear to be lower compared to the wrought counterpart, indicating a reduced resistance to cyclic loading. Several factors are responsible for a limited fatigue endurance, in particular process induced characteristics such as internal defects and surface roughness play a significant role. As explained earlier, MEAM is composed by three phases, shaping, debinding and sintering. The contribution of each phase on the fatigue resistance of the specimen is investigated in the present section for a better understanding of the weaknesses and strengths of the process. It is important to keep in mind that the specimens were tested in as-built conditions, meaning that neither mechanical nor chemical processes were applied to alter the surface. The arithmetical mean roughness parameter Ra ranges between 5 and 6 µm on the surfaces perpendicular to the building direction, while the side surfaces show an increased roughness. In [14,36], similar values of Ra were found for MEAM 316L specimens, while in [35], Ra is reported to be more than the double of this paper results. Indeed in [35], the observations of the fracture surfaces confirmed that the cracks nucleated from the superficial defects, while from the SEM pictures in Fig. 10 no crack starting from the outer surfaces are observed. As already mentioned in the previous section, crack initiation points are observed on the surfaces of the internal voids. From the optical microscope pictures collected in section 3.3, the voids induced by the deposition strategy appear to be close, with a regular spherical shape. The SEM pictures after fracture show a different morphology: in the first place it is possible to infer that the specimens are quite dense along the thickness. This is confirmed by the higher shrinkage factor that was calculated in section 3.1 along the vertical direction. In the detail of Fig. 10b, a stable fatigue crack growth area is highlighted. In this area the material appears perfectly homogeneous. The continuity of the material however is weakened at the interface of adjacent rasters, within the same layer. Being the infill strategy repetitive, those weak infra-layer areas are aligned through the thickness of the specimens, creating this characteristic pattern of alternating homogeneous areas and arrays of defect. Furthermore, these defects seem significantly larger compared to what obtained in section 3.2. This is possibly induced by the deformation of every single raster during tests. In a previous work, tensile tests of 316L dogbones obtained via MEAM were performed [31]. It was noticed that the specimens did not show a significant striction before fracture, and this was attributed to the non-continuous nature of the additive manufactured parts in which it is possible that a localized striction occurred in each raster. This possibly happened at a lower extent during the fatigue tests, especially in the specimens tested at high stress level. This localized deformation reduced the thickness of the rasters resulting in bigger infra-layer voids. In Fig. 11 the failure mechanism is described with the help of other SEM pictures of fracture surfaces. Two additional specimens were chosen with respect to the ones shown in the fractography section, therefore a new nomenclature is proposed with capital letters *A* and *B*. A miniature of the fatigue curve with indication of which are *A* and *B* is reported at the bottom of Fig. 11: specimen *A* was tested at high stress level, while specimen *B* failed in proximity of the fatigue limit. The surfaces are captured both from the front and the side view, showing an irregular segmented profile. Specimen *A* shows signs of necking, which is expected since it was tested at a stress level close to the tensile strength of the material. Fig. 11.c shows a schematic of a section of the specimens: the areas highlighted are the weak contact areas along rasters that create a favorite path for a crack to growth. The cracks are starting from the voids inside the specimens and alternating their growth direction along the rasters, taking advantage of weak points and defects to propagate. This is particularly clear from the pictures of specimen *B*, in which ductile fracture features corresponding to the final disruptive rupture are also visible close to the borders of the section. It is indeed possible to conclude that internal porosity is an issue that overcomes all the other possible defects of the specimens tested in the present work. As mentioned earlier, all the phases of MEAM give a contribution in the pore's creation. Among the multiple variables playing a role in this matter, some of them can be considered bounded. For example, in the present work a commercial filament was used, therefore among the several possible variables of the problems, it is convenient to consider the powder infill of the filament a bounded value. This is worthy to be explained since it was stated that the powder infill certainly has an impact on the density of the silver parts. Nevertheless, this can be detrimental during the printing phase, since a higher powder infill increases the viscosity and the fragility of the filament, resulting in a difficult extrusion [55]. What can be improved in the printing phase is the tuning of the parameters commanding the nozzle path while printing the infill. It seems that the outer walls are quite dense in comparison to the infill, therefore parameters such as the overlap percentage and extrusion width of the infill can be adjusted consequently. It might be a spontaneous choice to increase the flow rate multiplier, but this has been proven to be detrimental in terms of shape retention of the contour walls [19,31].

The sintering process is also important in the definition of some characteristics that affects the fatigue life of the specimens. The thermal process is responsible for the formation of small circular pores highlighted in Fig. 10a. This kind of porosity can be reduced increasing the sintering temperature and time, but this will in turn favor the grain growth. The grain size is related by the Hall-Petch effect to the strength of a metal, and it was proven that coarser microstructure increases the ductility [56]. Strength and ductility play a role in the fatigue behavior of metals, where materials with lower strength usually perform worse in HCF when compared with stronger counterparts. The proportionality between yield stress and fatigue limit was proven in [57]. Therefore, since the microstructure is already coarse, it is not advisable to intensify the sintering process, to avoid further growth. Applying post-treatment processes such as HIP might be studied. However, HIP can mostly help closing internal small pores, which is not the scenario presented in the present section. Nevertheless, post-processes can be considered to increase the densification of the specimens.

5. Conclusion

316L hourglass specimens were fabricated via MEAM and analyzed to increase the knowledge of the process-induced characteristics and to understand the relation to the fatigue behavior. As expected, the specimens shrunk considerably following the sintering process, with a linear reduction of 18.7, 17.3, and 20.7% respectively on the x-, y-, and z-axis. Despite the compaction of the metal powder and its diffusion, significant residual porosity was observed, with an average pore size of 37.2 μm. This result is particularly interesting when compared with the average grain size, which is 43.9 μm. The surface roughness of the fabricated specimens was assessed and the highest roughness was observed on the vertical surfaces, parallel to the building direction, with an average value of Ra = 7.7 μm. The Vickers microhardness is measured to be around 204 HV, a value expected for 316L stainless steel with coarse grains. Uniaxial fatigue tests were performed with a loading ratio of R = 0.1. The statistical fatigue limit according to ISO12107 is 137 MPa, even though it is possible to recognize an upper limit, around 175 MPa, considering the run-out specimens at 2 million cycles. These values are in the frame of the few available works about the fatigue behavior of 316L MEAM components but are not competitive in comparison to conventionally manufactured components. The main reason is attributed to the remaining porosity in the silver parts, whose origin must be imputed to the material deposition strategy during the printing phase. Several actions can be taken to improve the fatigue limit, such as improving the tuning of the printing parameters. In addition, application of post-treatment processes such as HIP to help close the pores can be investigated as future research on this topic. Nevertheless, this option is not to be preferred since the main advantages of the MEAM technique in terms of simplicity and cost-effectiveness can be compromised.

CRediT authorship contribution statement

Saveria Spiller: Writing – original draft, Visualization, Validation, Methodology, Investigation, Formal analysis, Data curation, Conceptualization. **Sondre Olsøybakk Kolstad:** Investigation, Formal analysis. **Nima Razavi:** Conceptualization, Methodology,

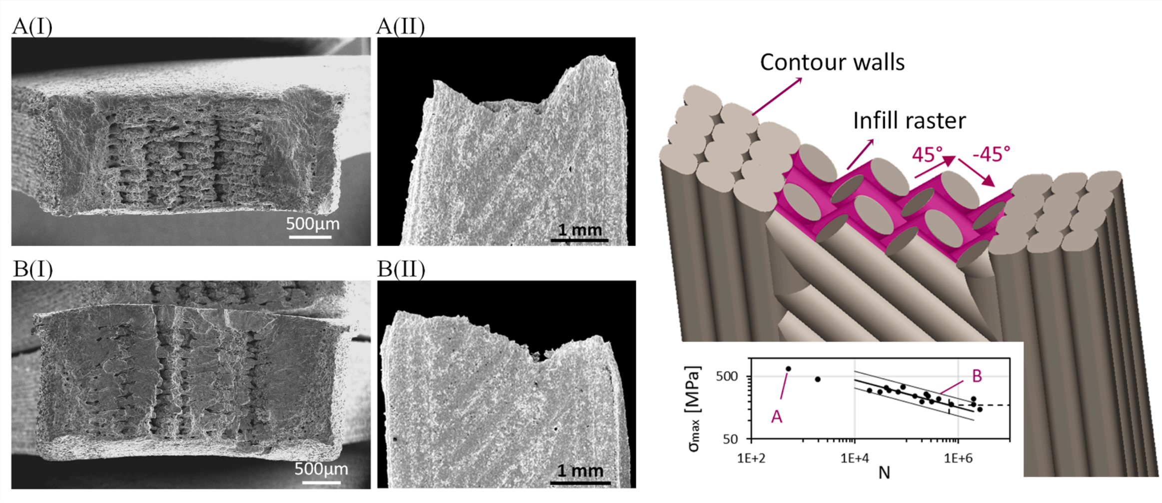

Fig. 11. Fracture surfaces of the specimen A and B that failed respectively at high and low stress levels, as indicated in the miniature of the fatigue curve reported at the bottom of the figure. The fracture surfaces were taken from the front view (pictures A(I) and B(I)) and from the side view (A(II) and B(II)). On the left, a fracture surface schematic is shown to illustrate how the irregular zig-zagged profile is created.

Investigation, Writing – review & editing, Supervision, Resources.

Declaration of Competing Interest

The authors declare that they have no known competing financial interests or personal relationships that could have appeared to influence the work reported in this paper.

Data availability

Data directly available in the paper.

References

[1] Cem S, Xiao B. A market assessment of additive manufacturing potential for the aerospace industry. J Manuf Process 2021;68:728–38. https://doi.org/10.1016/j.jmapro.2021.05.072.

[2] Jiménez M, Romero L, Dom IA, Dom M. Additive Manufacturing Technologies : An Overview about 3D Printing Methods and Future Prospects 2019;2019.

[3] Haghdadi N, Laleh M, Moyle M, Primig S. Additive manufacturing of steels : a review of achievements and challenges. J Mater Sci 2021;56:64–107. https://doi.org/10.1007/s10853-020-05109-0.

[4] Vafadar A, Guzzomi F, Rassau A, Hayward K. applied sciences Advances in Metal Additive Manufacturing : A Review of Common Processes , Industrial Applications , and Current Challenges 2021.

[5] Gonzalez-Gutierrez J, Cano S, Schuschnigg S, Kukla C, Sapkota J, Holzer C. Additive manufacturing of metallic and ceramic components by the material extrusion of highly-filled polymers: a review and future perspectives. Materials (Basel) 2018:11. https://doi.org/10.3390/ma11050840.

[6] Ramazani H, Kami A. Metal FDM, a new extrusion-based additive manufacturing technology for manufacturing of metallic parts: a review. Prog Addit Manuf 2022;7(4):609–26.

[7] Rane K, Strano M. A comprehensive review of extrusion-based additive manufacturing processes for rapid production of metallic and ceramic parts. Adv Manuf 2019;7(2):155–73.

[8] Jiang D, Ning F. Additive Manufacturing of 316L Stainless Steel by a Printing- Debinding-Sintering Method. Effects of Microstructure on Fatigue Property 2021;143:1–10. https://doi.org/10.1115/1.4050190.

[9] Liu B, Wang Y, Lin Z, Zhang T. Creating metal parts by Fused Deposition Modeling and Sintering. Mater Lett 2020;263:127252. https://doi.org/10.1016/j.matlet.2019.127252.

[10] Sadaf M, Bragaglia M, Nanni F. A simple route for additive manufacturing of 316L stainless steel via Fused Filament Fabrication. J Manuf Process 2021;67:141–50. https://doi.org/10.1016/j.jmapro.2021.04.055.

[11] Thompson Y, Gonzalez-Gutierrez J, Kukla C, Felfer P. Fused filament fabrication, debinding and sintering as a low cost additive manufacturing method of 316L stainless steel. Addit Manuf 2019;30:100861. https://doi.org/10.1016/j.addma.2019.100861.

[12] Kurose T, Abe Y, Santos MVA, Kanaya Y, Ishigami A, Tanaka S, et al. Influence of the layer directions on the properties of 316l stainless steel parts fabricated through fused deposition of metals. Materials (Basel) 2020;13(11):2493.

[13] Caminero MÁ, Romero A, Chacón JM, Núñez PJ, García-Plaza E, Rodríguez GP. Additive manufacturing of 316L stainless-steel structures using fused filament fabrication technology: mechanical and geometric properties. Rapid Prototyp J 2021;27:583–91. https://doi.org/10.1108/RPJ-06-2020-0120.

[14] Hassan W, Farid MA, Tosi A, Rane K, Strano M. The effect of printing parameters on sintered properties of extrusion-based additively manufactured stainless steel 316L parts. Int J Adv Manuf Technol 2021;114:3057–67. https://doi.org/10.1007/s00170-021-07047-w.

[15] Damon J, Dietrich S, Gorantla S, Popp U, Okolo B, Schulze V. Process porosity and mechanical performance of fused filament fabricated 316L stainless steel. Rapid Prototyp J 2019;25:1319–27. https://doi.org/10.1108/RPJ-01-2019-0002.

[16] Henry TC, Morales MA, Cole DP, Shumeyko CM, Riddick JC. Mechanical behavior of 17–4 PH stainless steel processed by atomic diffusion additive manufacturing. Int J Adv Manuf Technol 2021;114:2103–14. https://doi.org/10.1007/s00170-021-06785-1.

[17] Galati M, Minetola P. Analysis of density, roughness, and accuracy of the atomic diffusion additive manufacturing (ADAM) process for metal parts. Materials (Basel) 2019:12. https://doi.org/10.3390/ma1224122.

[18] Gonzalez-Gutierrez J, Arbeiter F, Schlauf T, Kukla C, Holzer C. Tensile properties of sintered 17–4PH stainless steel fabricated by material extrusion additive manufacturing. Mater Lett 2019;248:165–8. https://doi.org/10.1016/j.matlet.2019.04.024.

[19] Godec D, Cano S, Holzer C, Gonzalez-Gutierrez J. Optimization of the 3D printing parameters for tensile properties of specimens produced by fused filament fabrication of 17–4PH stainless steel. Materials (Basel) 2020:13. https://doi.org/10.3390/ma13030774.

[20] Suwanpreecha C, Seensattayawong P, Vadhanakovint V, Manonukul A. Influence of Specimen Layout on 17–4PH (AISI 630) Alloys Fabricated by Low-Cost Additive Manufacturing. Metall Mater Trans A Phys Metall Mater Sci 2021;52:1999–2009. https://doi.org/10.1007/s11661-021-06211-x.

[21] Alkindi T, Alyammahi M, Susantyoko RA, Atatreh S. The effect of varying specimens' printing angles to the bed surface on the tensile strength of 3D-printed 17–4PH stainless-steels via metal FFF additive manufacturing. MRS Commun 2021;11:310–6. https://doi.org/10.1557/s43579-021-00040-0.

[22] Thompson Y, Polzer M, Gonzalez-Gutierrez J, Kasian O, Heckl JP, Dalbauer V, et al. Fused Filament Fabrication-Based Additive Manufacturing of Commercially Pure Titanium. Adv Eng Mater 2021;23(12):2100380.

[23] Shaikh MQ, Graziosi S, Atre SV. Supportless printing of lattice structures by metal fused filament fabrication (MF3) of Ti-6Al-4V: design and analysis. Rapid Prototyp J 2021;27:1408–22. https://doi.org/10.1108/RPJ-01-2021-0015.

[24] Singh P, Balla VK, Tofangchi A, Atre SV, Kate KH. Printability studies of Ti-6Al-4V by metal fused filament fabrication (MF3). Int J Refract Met Hard Mater 2020;91:105249. https://doi.org/10.1016/j.ijrmhm.2020.105249.

[25] Singh P, Balla VK, Gokce A, Atre SV, Kate KH. Additive manufacturing of Ti-6Al-4V alloy by metal fused filament fabrication (MF3): producing parts comparable to that of metal injection molding. Prog Addit Manuf 2021;6(4):593–606.

[26] Lengauer W, Duretek I, Fürst M, Schwarz V, Gonzalez-Gutierrez J, Schuschnigg S, et al. Fabrication and properties of extrusion-based 3D-printed hardmetal and cermet components. Int J Refract Met Hard Mater 2019;82:141–9.

[27] Bose A, Schuh CA, Tobia JC, Tuncer N, Mykulowycz NM, Preston A, et al. Traditional and additive manufacturing of a new Tungsten heavy alloy alternative. Int J Refract Met Hard Mater 2018;73:22–8.

[28] Dehdari Ebrahimi N, Ju YS. Thermal conductivity of sintered copper samples prepared using 3D printing-compatible polymer composite filaments. Addit Manuf 2018;24:479–85. https://doi.org/10.1016/j.addma.2018.10.025.

[29] Rane K, Petrò S, Strano M. Evolution of porosity and geometrical quality through the ceramic extrusion additive manufacturing process stages. Addit Manuf 2020;32:101038. https://doi.org/10.1016/j.addma.2020.101038.

[30] Abel J, Scheithauer U, Janics T, Hampel S, Cano S, Müller-Köhn A, et al. Fused filament fabrication (FFF) of metal-ceramic components. J Vis Exp 2019;(143). https://doi.org/10.3791/57693.

[31] Spiller S, Olsøybakk S, Mohammad S, Razavi J. Fabrication and characterization of 316L stainless steel components printed with material extrusion additive manufacturing. Procedia Struct Integr 2022;42:1239–48. https://doi.org/10.1016/j.prostr.2022.12.158.

[32] Wagner G, Williams CB. Effect of Particle Size Distribution on Powder Packing and Sintering in Binder Jetting Additive Manufacturing of Metals 2017;139:1–6. https://doi.org/10.1115/1.4036640.

[33] Spiller S, Berto F, Javad Razavi SM. Mechanical behavior of Material Extrusion Additive Manufactured components: an overview. Procedia Struct Integr 2022;41:158–74. https://doi.org/10.1016/j.prostr.2022.05.018.

[34] Rosnitschek T, Tremmel S, Seefeldt A, Alber-Laukant B, Neumeyer T, Altstädt V. Correlations of geometry and infill degree of extrusion additively manufactured 316l stainless steel components. Materials (Basel) 2021;14. https://doi.org/10.3390/ma14185173.

[35] Suwanpreecha C, Songkuea S, Linjee S, Muengto S, Bumrungpon M, Manonukul A. Tensile and axial fatigue properties of AISI 316 L stainless steel fabricated by materials extrusion additive manufacturing. Mater Today Commun 2023;35:105667. https://doi.org/10.1016/j.mtcomm.2023.105667.

[36] Kedziora S, Decker T, Museyibov E, Morbach J, Hohmann S, Huwer A, et al. Strength Properties of 316L and 17-4 PH Stainless Steel Produced with Additive Manufacturing 2022.

[37] Sanaei N, Fatemi A. Defects in additive manufactured metals and their effect on fatigue performance : A state-of-the-art review. Prog Mater Sci 2021;117:100724. https://doi.org/10.1016/j.pmatsci.2020.100724.

[38] Becker TH, Kumar P, Ramamurty U. Fracture and fatigue in additively manufactured metals. Acta Mater 2021;219:117240.

[39] Kumar P, Jayaraj R, Suryawanshi J, Satwik UR, Mckinnell J, Ramamurty U. Acta Materialia Fatigue strength of additively manufactured 316L austenitic stainless steel. Acta Mater 2020;199:225–39. https://doi.org/10.1016/j.actamat.2020.08.033.

[40] Zhang M, Sun C, Zhang X, Chin P, Wei J, Hardacre D. Materials Science & Engineering A Fatigue and fracture behaviour of laser powder bed fusion stainless steel 316L : Influence of processing parameters. Mater Sci Eng A 2017;703:251–61. https://doi.org/10.1016/j.msea.2017.07.071.

[41] Spierings AB, Starr TL, Ag I. Fatigue performance of additive manufactured metallic parts 2013;2:88–94. https://doi.org/10.1108/13552541311302932.

[42] Shrestha R, Simsiriwong J, Shamsaei N. Fatigue behavior of additive manufactured 316L stainless steel parts : Effects of layer orientation and surface roughness. Addit Manuf 2019;28:23–38. https://doi.org/10.1016/j.addma.2019.04.011.

[43] Nafar J, Jaberi O, Remes H. Influence of internal and surface defects on the fatigue performance of additively manufactured stainless steel 316L. Int J Fatigue 2022;163:107025. https://doi.org/10.1016/j.ijfatigue.2022.107025.

[44] Wickramasinghe S, Do T, Tran P. FDM-Based 3D Printing of Polymer and Associated Composite. A Review on Mechanical Properties 2020.

[45] Hsiang Loh G, Pei E, Gonzalez-Gutierrez J, Monzón M. An overview of material extrusion troubleshooting. Appl Sci 2020;10(14):4776.

[46] German RM. Thermodynamics of sintering. Woodhead Publishing Limited; n.d. https://doi.org/10.1533/9781845699949.1.110.

[47] Gong H, Snelling D, Kardel K, Carrano A. Comparison of Stainless Steel 316L Parts Made by FDM- and SLM-Based Additive Manufacturing Processes. Jom 2019;71:880–5. https://doi.org/10.1007/s11837-018-3207-3.

[48] BASF Ultrafuse 316L n.d.:Ultrafuse 316L. https://www.ultrafusefff.com/product-category/metal/ultrafuse-316l/.

[49] Tronvoll SA, Vedvik NP, Elverum CW, Welo T. A new method for assessing anisotropy in fused deposition modeled parts using computed tomography data 2019;105(1-4):47–65.

[50] Yang N, Yee J, Zheng B, Gaiser K, Reynolds T, Clemon L, et al. Process-Structure-Property Relationships for 316L Stainless Steel Fabricated by Additive Manufacturing and Its Implication for Component Engineering. J Therm Spray Technol 2017;26(4):610–26.

[51] Dowling NE, Calhoun CA, Arcari A. Mean stress effects in stress-life fatigue and the Walker equation. Fatigue Fract Eng Mater Struct 2009;32:163–79. https://doi.org/10.1111/j.1460-2695.2008.01322.x.

[52] Roland T, Retraint D, Lu K, Lu J. Fatigue life improvement through surface nanostructuring of stainless steel by means of surface mechanical attrition treatment 2006;54(11):1949–54.

[53] Mower TM, Long MJ. Materials Science & Engineering A Mechanical behavior of additive manufactured, powder-bed laser-fused materials. Mater Sci Eng A 2016;651:198–213. https://doi.org/10.1016/j.msea.2015.10.068.

[54] Huang HW, Wang ZB, Lu J, Lu K. Fatigue behaviors of AISI 316L stainless steel with a gradient nanostructured surface layer 2015;87:150–60.

[55] Cerejo F, Gatões D, Vieira MT. Optimization of metallic powder filaments for additive manufacturing extrusion (MEX). Int J Adv Manuf Technol 2021;115:2449–64. https://doi.org/10.1007/s00170-021-07043-0.

[56] Qin W, Li J, Liu Y, Kang J, Zhu L, Shu D, et al. Effects of grain size on tensile property and fracture morphology of 316L stainless steel. Mater Lett 2019;254:116–9.

[57] Mutoh Y, Radhakrishnan VM. Effect of yield stress and grain size on threshold and fatigue limit. J Eng Mater Technol Trans ASME 1986;108:174–8. https://doi.org/10.1115/1.3225857.